GEOPHYSICS, VOL. 81, NO. 6 (NOVEMBER-DECEMBER 2016); P. IM119–IM126, 9 FIGS.
10.1190/GEO2016-0250.1

Methods to compute salt likelihoods and extract salt boundaries from 3D seismic images

Xinming Wu[1]

ABSTRACT

Salt body interpretation is important for building subsurface models and interpreting seismic horizons and faults that might be truncated by the salt. Salt interpretation often includes two steps: highlighting salt boundaries with a salt attribute image and extracting salt boundaries from the attribute image. Although both steps have been automated to some extent, salt interpretation today typically still requires significant manual effort. From a 3D seismic image, I first efficiently compute a salt likelihood image, in which the ridges of likelihood values indicate locations of salt boundaries. I then extract salt samples on the ridges, and these samples can be directly connected to construct salt boundaries in cases when salt structures are simple and the boundaries are clean. In more complicated cases, these samples may be noisy and incomplete, and some of the samples can be outliers unrelated to salt boundaries. Therefore, I have developed a method to accurately fit noisy salt samples, reasonably fill gaps, and handle outliers to simultaneously construct multiple salt boundaries. In this step of constructing salt boundaries, I also have developed a convenient way to incorporate human interactions to obtain more accurate salt boundaries in especially complicated cases. I have performed the methods of computing salt likelihoods and constructing salt surfaces using a 3D seismic image containing multiple salt bodies.

INTRODUCTION

Salt boundaries, together with seismic horizons (Wu and Zhong, 2012; Wu and Hale, 2013, 2015b), faults (Hale, 2013; Wu and Hale, 2016), and unconformities (Wu and Hale, 2015a) are important aspects of geologic structures that can be extracted from seismic images. To extract salt bodies from a seismic image, we often need to distinguish salt boundaries from the other structures that are also present in the image. Therefore, in extracting salt boundaries, we often first compute a salt attribute image, in which only the salt boundaries are most prominent, as shown in Figure 1a.

In a seismic image (background image in Figure 1a), seismic reflections inside a salt are typically weak and chaotic, whereas those outside are often stronger and more consistent. Based on these observations, several commonly used methods have been proposed to compute different types of salt attributes to highlight salt boundaries. Some methods (Jing et al., 2007; Aqrawi et al., 2011; Asjad and Mohamed, 2015) propose to compute amplitude discontinuity attributes using edge-detection-based techniques such as Sobel filters. Others compute texture attributes (Berthelot et al., 2013; Hegazy and Alregib, 2014; Wang et al., 2015), seismic reflection dip attributes (Halpert and Clapp, 2008), or equivalently, reflection normal vector field attributes (Haukås et al., 2013). Some authors (Halpert et al., 2014; Amin and Deriche, 2015) suggest using multiple attributes combined together for highlighting salt boundaries because a single attribute might be insufficient to provide a good detection.

After computing a salt attribute image, salt boundaries are then extracted from such an image. Lomask et al. (2007) and Ramirez et al. (2016) consider salt boundary extraction as an image segmentation problem and apply the normalized cuts (Shi and Malik, 2000) and sparse representation (Donoho et al., 1998), respectively, to find salt boundaries. Zhang and Halpert (2012) and Haukås et al. (2013) propose to use active-contour-based methods that start with some initial shape and then gradually and automatically deform it to fit a salt boundary. Although automatic methods have been proposed in this step for extracting salt boundaries, human interaction often is still desirable for more complicated cases to obtain more accurate results, as discussed by Zhang and Halpert (2012) and Halpert et al. (2014).

In this paper, I first propose to compute an image of salt likelihood, defined as the variation of seismic reflector linearity (2D) or planarity (3D), to highlight salt boundaries, as shown in Figure 1a. Because salt boundaries are not as thick as the features apparent in

Manuscript received by the Editor 12 May 2016; revised manuscript received 6 July 2016; published online 23 September 2016.
[1]Colorado School of Mines, Golden, Colorado, USA. E-mail: xinwucwp@gmail.com.

the salt likelihood image in Figure 1a, I keep only the values on the ridges of salt likelihood and set values elsewhere to be zero, to obtain a thinned salt likelihood image (Figure 1b). Most of the nonzero samples in Figure 1b are located at the salt boundary; however, some of them are outliers unrelated to salt boundaries, and some samples are missing at the salt boundary. This means that it might be difficult to obtain accurate and complete salt boundaries by directly linking these nonzero salt samples. Therefore, I then propose to compute a salt indicator image such that the zero contour of this indicator image will accurately fit noisy salt samples, reasonably fill gaps and handle outliers, such as the one denoted by magenta in Figure 1c. This method simultaneously extracts multiple salt boundaries by simply extracting all the zero contours of the indicator image. In computing the salt indicator image, I also propose a convenient way to incorporate human interactions into the method for extracting more accurate salt boundaries in more complicated cases. These human interactions can be points, segments, or patches of manually interpreted salt boundaries.

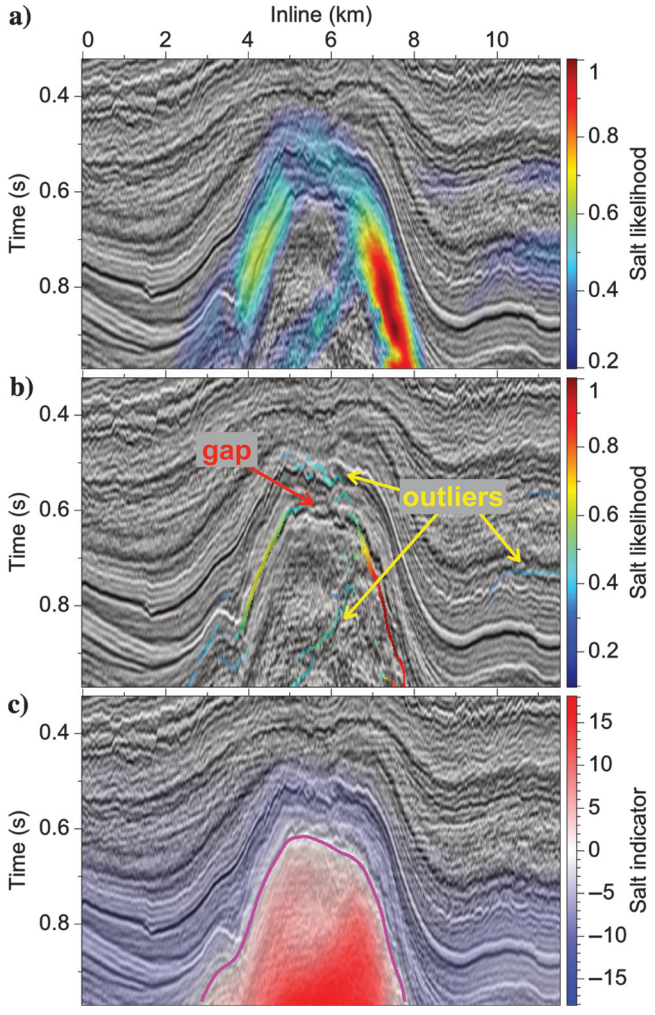

Figure 1. A seismic image is displayed with a salt likelihood image (a) before and (b) after thinning. The thinned likelihood image, with nonzero samples only on the ridges of the salt likelihood image (a), is then used to compute a salt indicator image (c), in which the zero contour (magenta curve) represents the salt boundary.

SALT ATTRIBUTE

To extract salt boundaries from a seismic image, a useful first step is to compute a second attribute image that highlights locations of the salt boundaries. I propose to use an image of salt likelihood, defined as the variation of reflector linearity (2D) or planarity (3D) in a seismic image, to detect salt boundaries.

Seismic linearity and planarity

In a seismic image, seismic reflectors often appear linear (2D) or planar (3D) outside salt bodies but are weak and incoherent within the salt bodies. Therefore, attributes based on structure (Haukås et al., 2013) or texture (Berthelot et al., 2013; Hegazy and Alregib, 2014; Wang et al., 2015) of reflectors are often used to detect salts.

The attribute I use to detect salt boundaries is derived from seismic structure tensors (Van Vliet and Verbeek, 1995; Weickert, 1997; Fehmers and Höcker, 2003), which are smoothed outer products of image gradients:

$$\mathbf{T} = \langle \mathbf{g}\mathbf{g}^{\mathsf{T}} \rangle, \tag{1}$$

where $\mathbf{g}$ represents the seismic image gradient vector (column vector) computed for each image sample. I efficiently compute the image gradients using recursive Gaussian derivative filters (Deriche, 1993; Van Vliet et al., 1998; Hale, 2006) with radius $\sigma = 1$ (sample) and $\langle \cdot \rangle$ denotes smoothing for each element of the outer product or structure tensor. This smoothing, often implemented as a Gaussian filter, helps to construct structure tensors with more stable estimations of seismic reflector orientations.

Each structure tensor $\mathbf{T}$, constructed for each image sample, is a symmetric positive semidefinite matrix. For a 2D seismic image (Figures 1a and 2a), a structure tensor is a 2×2 matrix with eigendecomposition

$$\mathbf{T} = \lambda_u \mathbf{u}\mathbf{u}^{\mathsf{T}} + \lambda_v \mathbf{v}\mathbf{v}^{\mathsf{T}}, \tag{2}$$

where λ_u and λ_v are the eigenvalues corresponding to eigenvectors $\mathbf{u}$ and $\mathbf{v}$ of $\mathbf{T}$. As shown by Fehmers and Höcker (2003), the eigenvectors $\mathbf{u}$ and $\mathbf{v}$ provide estimations of reflector orientations. If we label the eigenvalues $\lambda_u \geq \lambda_v \geq 0$, then the corresponding eigenvectors $\mathbf{u}$ are perpendicular to locally linear features in an image, and the eigenvectors $\mathbf{v}$ are parallel to such features.

As discussed by Hale (2009), the eigenvalues λ_u and λ_v provide measures of isotropy and linearity of structures apparent in the image. The linearity l ($0 \leq l \leq 1$) for each image sample can be computed by the following ratio of the eigenvalues (Hale, 2009):

$$l = \frac{\lambda_u - \lambda_v}{\lambda_u}. \tag{3}$$

As shown in Figure 2b, linearities are close to one for samples in areas with continuous and coherent reflectors, but they are nearly zero in areas with chaotic or noisy reflectors.

To measure the linearity of structures with different scales, we can vary the smoothing ($\langle \cdot \rangle$) extents in equation 1 for constructing structure tensors. For local and subtle structures, we want to apply weak smoothing with small half-width σ as shown in Figure 2b ($\sigma = 2$ [samples]). For more global structures such as salts, we want to apply stronger smoothing with larger half-width, for example

$\sigma = 80$ (samples) in Figure 3a. However, we do not expect to smooth across salt boundaries when constructing structure tensors; therefore, we may want to apply a structure-oriented smoothing (Hale, 2009) with large extent in Figure 3b, instead of an isotropic Gaussian filter in Figure 3a. This structure-oriented smoothing filter has a comparable smoothing extent to that of the Gaussian filter.

As shown in Figure 3a, stronger smoothing yields more continuous and smoother linearities than those in Figure 3b and also blurs the discontinuities near the salt boundary. As shown in Figure 3b, the structure-oriented smoothing filter also yields smooth linearity values within and outside the salt but preserves the discontinuity of linearity near the salt boundary.

For each sample in a 3D seismic image, such as the one shown in Figure 4a, we can use equation 1 with the same structure-oriented smoothing filter to construct a structure tensor, which is a 3×3 matrix with the following eigendecomposition:

$$\mathbf{T} = \lambda_u \mathbf{u}\mathbf{u}^\top + \lambda_v \mathbf{v}\mathbf{v}^\top + \lambda_w \mathbf{w}\mathbf{w}^\top. \tag{4}$$

Similarly, we label the eigenvalues and corresponding eigenvectors so that $\lambda_u \geq \lambda_v \geq \lambda_w$. As discussed by Hale (2009), we can define planarity p ($0 \leq p \leq 1$) in 3D using the eigenvalues:

$$p = \frac{\lambda_u - \lambda_v}{\lambda_u}. \tag{5}$$

Figure 4b shows such a planarity image displayed as translucent colors overlaid with the 3D seismic image. Similar to the linearity in 2D as shown in Figure 3b, the planarity values are relatively high outside the salt bodies but are low within the salt.

Salt likelihood

As shown in Figures 3b and 4b, the linearity and planarity values decrease most significantly near the salt boundary toward the interior of the salt. Therefore, I define salt likelihood, a measure of linearity or planarity variation in direction perpendicular to seismic reflectors, to highlight out salt boundaries:

$$h = \begin{cases} \nabla l \cdot \mathbf{u}_s, & \text{for 2D} \\ \nabla p \cdot \mathbf{u}_s, & \text{for 3D} \end{cases}, \tag{6}$$

where $\mathbf{u}_s$ are the unit vectors computed for all image samples and are perpendicular to seismic reflectors. These vectors $\mathbf{u}_s$ are the eigenvectors corresponding to the maximum eigenvalues of the structure tensors (equation 1) constructed from the seismic images (Figures 2a and 4a) with Gaussian smoothing filters. For the linearity or planarity

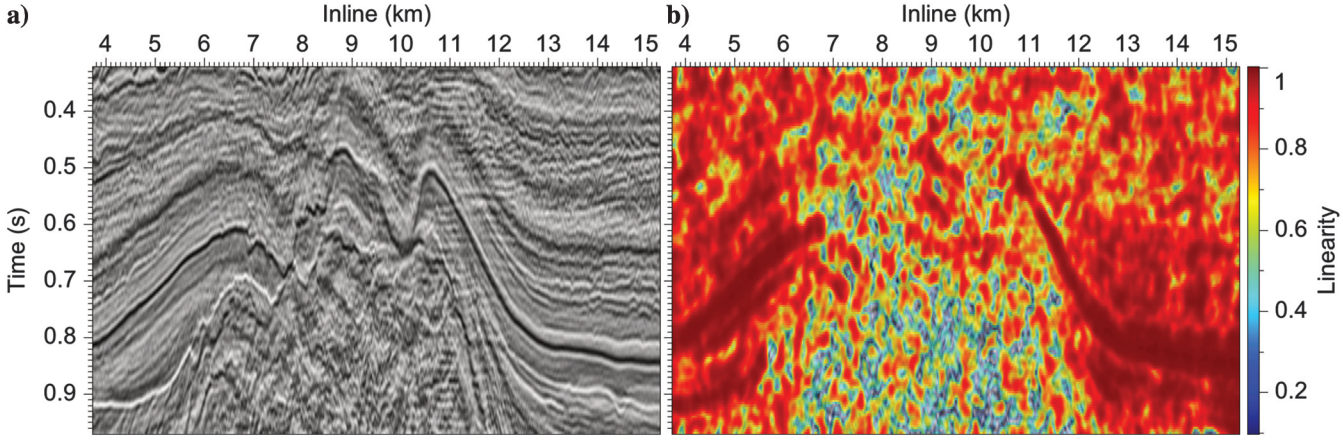

Figure 2. A seismic image (a) displayed with linearity (b) computed using isotropic Gaussian smoothing ($\sigma = 2$ [samples]).

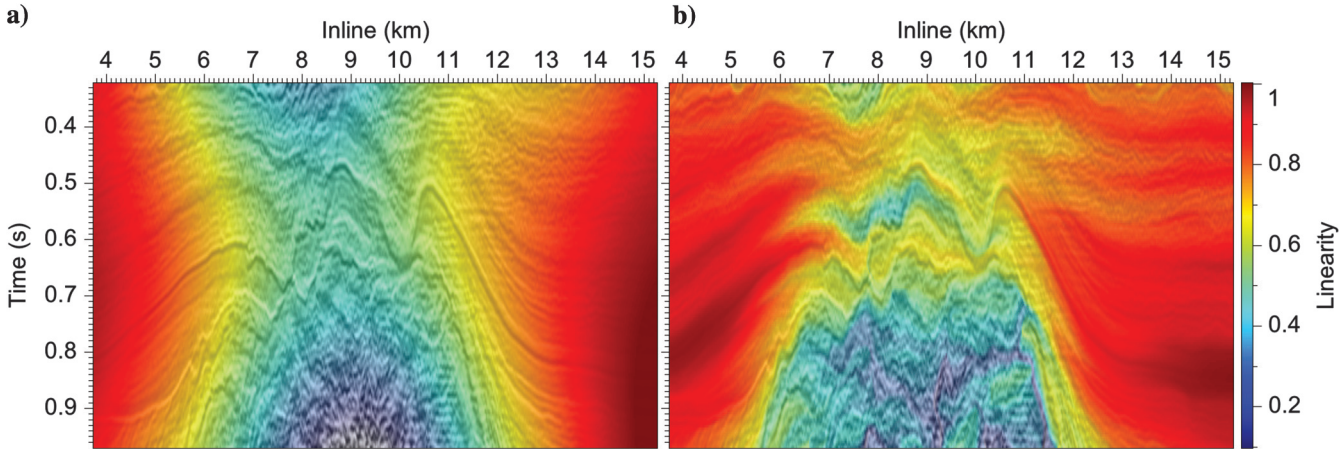

Figure 3. Two images of linearities computed using (a) an isotropic Gaussian filter and (b) a structure-oriented smoothing filter, respectively. The smoothing extent of the latter filter is comparable to that of the former with $\sigma = 80$ (samples).

gradient, I apply Gaussian derivative filters ($\sigma = 8$ [samples]) to the linearity or planarity image vertically and horizontally to approximate the corresponding components of the gradient.

Figures 5a and 6a are such 2D and 3D salt likelihood images after normalization. The salt likelihood values are displayed with translucent colors and overlaid with the seismic images. In these images, high likelihood values indicate the locations of the salt boundary. However, we do not expect salt boundaries to be as thick as the features apparent in the salt likelihood image. Therefore, I keep only the values on the ridges of salt likelihood and set values elsewhere to be zero, to obtain a thinned salt likelihood image shown in Figure 5b. In 3D, a thinned salt likelihood image can be displayed as salt sam-

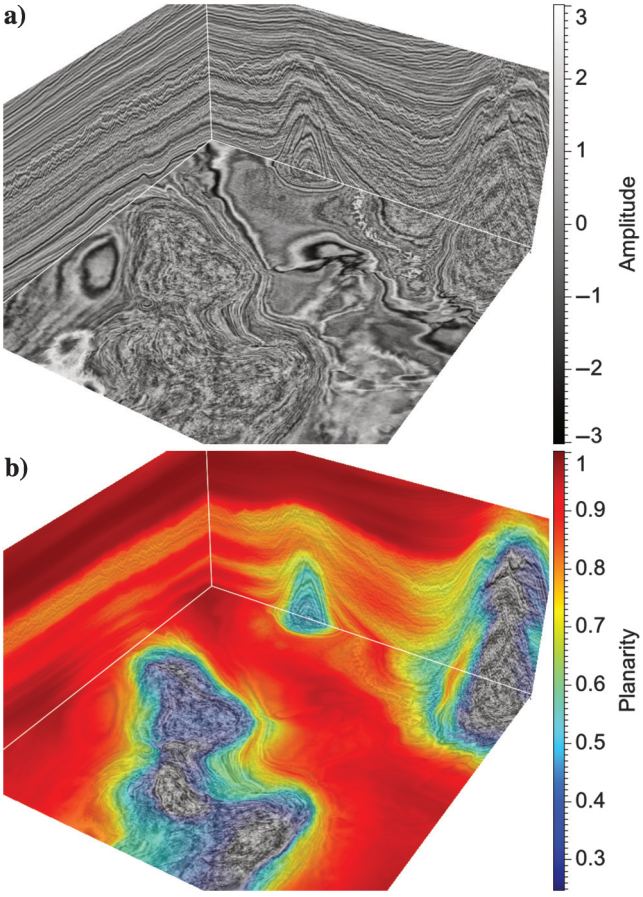

Figure 4. A seismic image (a) displayed with planarity (b), which is displayed as a translucent color.

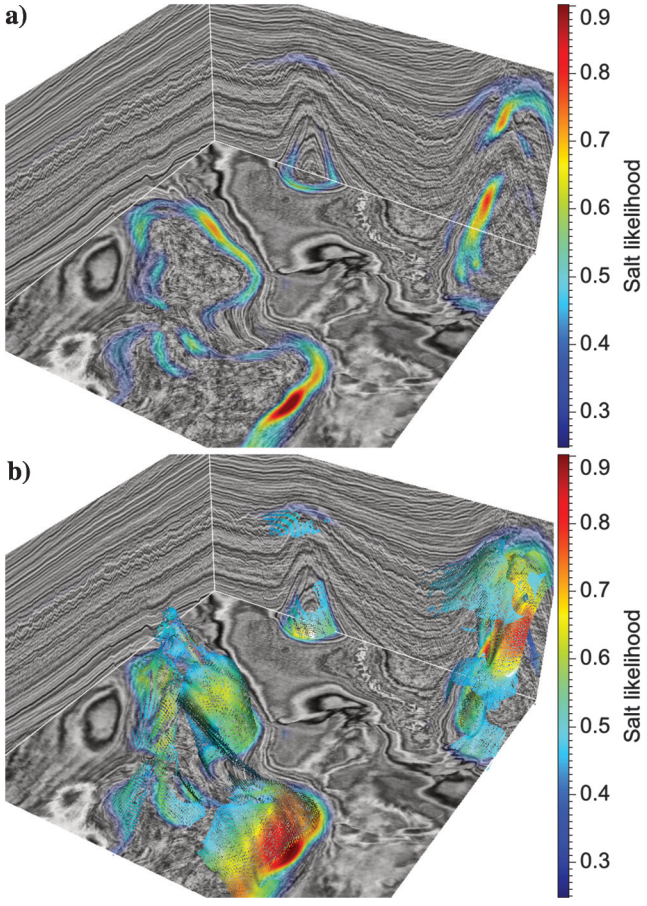

Figure 6. (a) Salt likelihoods are displayed as translucent colors overlaid with the seismic image. (b) Salt samples, colored by salt likelihoods, are extracted on the ridges of the likelihood image.

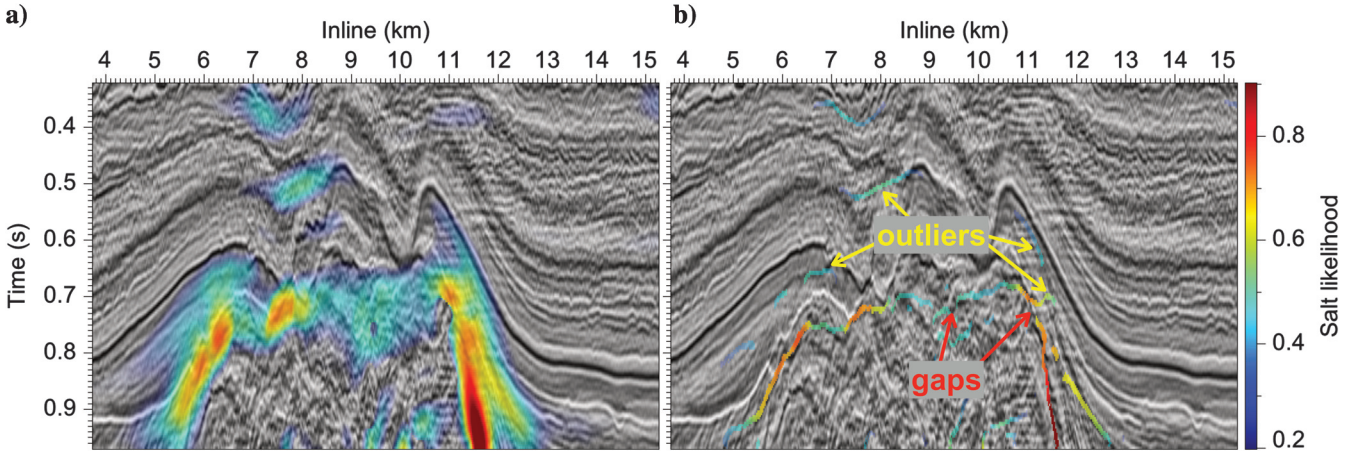

Figure 5. A seismic image displayed with salt likelihoods (a) before and (b) after thinning.

ples colored by likelihood values, as shown in Figure 6b. These samples are located within the sampling grid of the 3D seismic image.

After thinning, most salt samples, especially those with high likelihood values, are located at salt boundaries. Most samples are aligned and appear to form segments (Figure 5b) or patches (Figure 6b) of salt boundaries. These samples, however, are not connected to form salt boundaries. Moreover, some noisy or outlier samples, which do not belong to a salt boundary, are apparent in the thinned salt likelihood images. In addition, some samples are missing at the salt boundaries.

EXTRACTING SALT BOUNDARIES

It might be difficult to directly connect the salt samples (samples with nonzero salt likelihood values) in the thinned salt likelihood image to construct salt boundaries because of the noisy samples in the image and potential gaps apparent at the salt boundaries. Therefore, I propose a method to compute another salt indicator function from the salt likelihood image, and then extract multiple closed and smooth salt boundaries by extracting zero contours of the indicator function. Human interactions can be conveniently incorporated into the method to compute more reliable salt indicator functions for complicated examples in which the salt likelihood images fail to correctly detect salt boundaries.

Salt indicator function

Construction of salt boundaries from salt samples (Figures 5b and 6b) is similar to the problem of surface reconstruction from scattered points, which is well-studied in computer graphics. Numerous methods (Kazhdan et al., 2006; Guennebaud and Gross, 2007; Lipman et al., 2007; Kazhdan and Hoppe, 2013; Berger et al., 2014) have been proposed to compute reasonable surfaces that fit the given sparse points.

I propose a method, similar to the one developed by Kazhdan and Hoppe (2013), to accurately fit noisy salt samples, reasonably fill gaps, and handle outliers to simultaneously construct multiple salt boundary surfaces. In this method, I first compute a vector field $\mathbf{u}_p(\mathbf{x})$ that contains the eigenvectors corresponding to the maximum eigenvalues of the structure tensors (equation 1) constructed from the linearity (Figure 3b) or planarity (Figure 4b) image. I then use this vector field $\mathbf{u}_p(\mathbf{x})$, as well as the salt samples (Figures 5b and 6b), to compute another salt indicator function $f(\mathbf{x})$ by solving the following equations:

$$\begin{aligned} h(\mathbf{x})\nabla f(\mathbf{x}) &\approx h(\mathbf{x})\mathbf{u}_p(\mathbf{x}) \\ h(\mathbf{x_k})f(\mathbf{x}_k) &\approx 0, \end{aligned} \tag{7}$$

where ∇ is the gradient operator, $\mathbf{x}_k$ represent the 2D or 3D positions of salt samples as shown in Figures 5b and 6b, $h(\mathbf{x})$ represents a 2D or 3D salt likelihood image, as shown in Figures 5a and 6a, and is used to

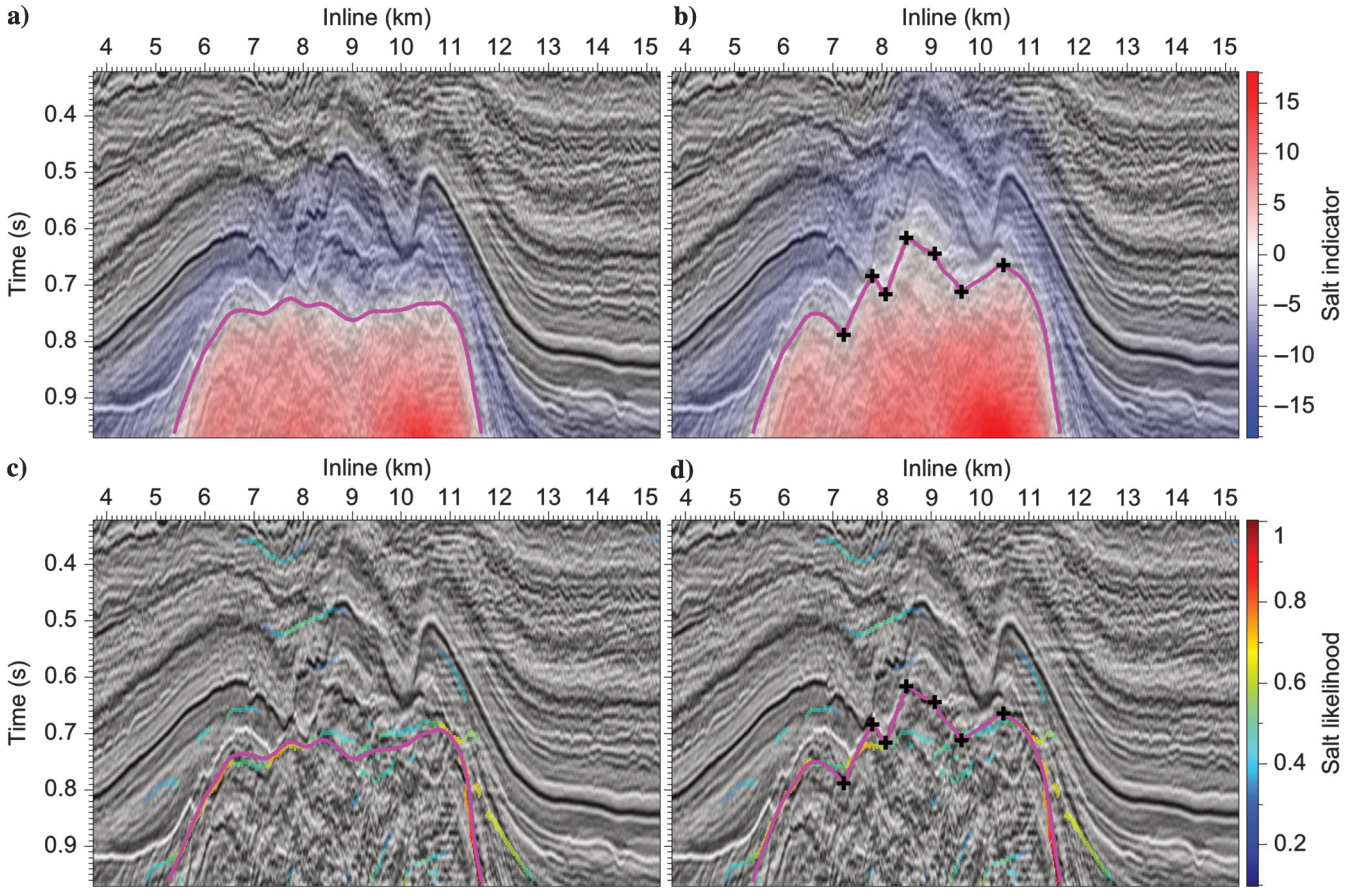

Figure 7. The thinned salt likelihood image (Figure 5b) and a normal vector field estimated from the linearity image (Figure 3b) are used to compute salt indicator images (a) with and (b) without control points (black plus marks). Zero contours (magenta curves) of the salt indicator images represent salt boundaries, which reasonably fit salt samples and fill holes (missing salt samples) as shown in panels (c and d).

weight the equations. The first equation implies that we expect to find a scalar function $f(\mathbf{x})$ whose gradients best match the vector field $\mathbf{u}(\mathbf{x})_p$, whereas the second one means that we expect the scalar function to be zero at the salt boundaries. Therefore, after solving for such a scalar function, we expect the zero contours of this function to coincide with the salt boundaries.

Equation 7 can be represented in the matrix-vector notation as

$$\begin{bmatrix} \tilde{\mathbf{H}} \\ \mathbf{HG} \end{bmatrix} \mathbf{f} \approx \begin{bmatrix} \mathbf{0} \\ \mathbf{Hb} \end{bmatrix}. \tag{8}$$

For a 3D image with N samples, $\mathbf{f}$ is a $N \times 1$ vector representing the unknown function $f(\mathbf{x})$; $\mathbf{G}$ is a $3N \times N$ matrix representing a finite-difference approximation of the gradient operator; $\mathbf{H}$ is a $3N \times 3N$ diagonal matrix with salt likelihood values on the diagonal entries; $\tilde{\mathbf{H}}$ is also a $N \times N$ diagonal matrix but with zeros on most diagonal entries and nonzero values (salt likelihoods) only on the entries corresponding to the salt samples ($\mathbf{x}_k$); and $\mathbf{b}$ is a $3N \times 1$ vector containing the 3C of the vector field $\mathbf{u}_p$.

In this problem, we have more equations than unknowns; therefore, we might compute a least-squares solution of equations 8 by solving the normal equation

$$(\mathbf{G}^\top\mathbf{H}^\top\mathbf{HG} + \tilde{\mathbf{H}}^\top\tilde{\mathbf{H}})\mathbf{f} = \mathbf{G}^\top\mathbf{H}^\top\mathbf{Hb}. \tag{9}$$

In solving this equation, I do not explicitly form the matrices above. The matrix $\mathbf{G}^\top\mathbf{H}^\top\mathbf{HG} + \tilde{\mathbf{H}}^\top\tilde{\mathbf{H}}$ on the left side is symmetric positive definite; therefore, I solve the equation using a conjugate gradient (CG) method that requires only the computation of matrix-vector products.

By solving equation 9, I compute two 2D salt indicator functions that are displayed in translucent blue-white-red colors in Figures 1c and 7a. The values of the indicator functions smoothly increase from negative (blue) to positive (red) in directions toward interior of the salt. From the computed indicator functions, zero contours (magenta curves in Figures 1c and 7a) are extracted to represent salt boundaries. As shown in Figure 7c, the extracted zero contour (magenta curve) reasonably fits the salt samples, fills holes (missing salt samples), and matches well with the apparent salt boundary.

Figure 8a shows a 3D salt indicator function computed with the method discussed above, which is displayed as blue-white-red colors overlaid on the 3D seismic image. We can observe that the values of the function are smooth everywhere, negative outside the salts, and positive inside the salts. With this salt indicator function, I simultaneously obtain all the salt boundary surfaces, displayed by magenta surfaces in Figure 8b, by extracting zero contours of the function. To compute these zero contours, I use the efficient marching cubes algorithm (Lorensen and Cline, 1987). In Figure 9, these extracted surfaces (colored by magenta) are displayed together with the salt samples (colored by salt likelihoods). We observe that these surfaces reasonably fill holes, fit most salt samples with high likelihoods, and are not corrupted by outlier samples that do not correspond to any salt boundaries.

Human interaction

The methods discussed above work well to extract reasonable salt boundaries for the examples in this paper. However, human interaction from experienced interpreters is still desirable for the salt boundary extraction, especially for more complicated examples in which a salt attribute like the salt likelihood cannot provide a good detection of salt boundaries. Here, I propose a convenient

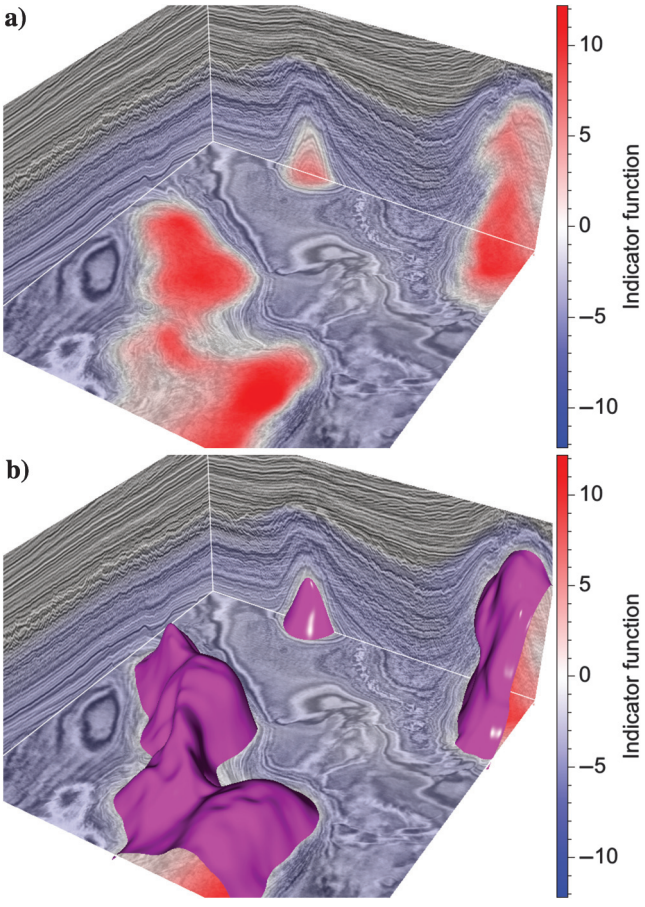

Figure 8. The salt samples (Figure 6b) and a normal vector field estimated from the planarity image (Figure 4b) are used to compute a salt indicator image that is displayed as translucent color in panel (a). Zero contour surfaces (colored by magenta in [b]) of this indicator image represent salt boundary surfaces.

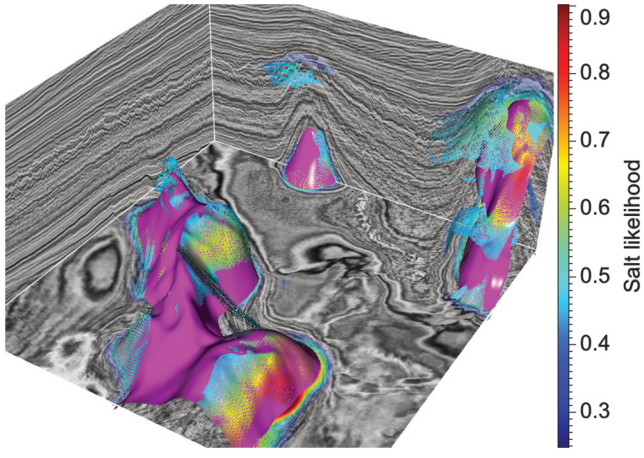

Figure 9. The extracted salt surfaces (colored by magenta) reasonably fill holes, well fit most salt samples (colored by salt likelihoods), especially those with high likelihoods, and are not deviated by outlier salt samples.

way to incorporate human interaction into the method for computing salt indicator functions.

Suppose we have a set of manually picked control points $\mathbf{x}_i, i = 1, 2, \ldots, n$, and we expect the extracted salt boundary to exactly pass through these points. This means that we expect the salt indicator function to be zero at the control points $f(\mathbf{x}_i) = 0$. Therefore, we might want to use these points as hard constraints and solve the following simple constrained optimization problem:

$$\min \|\tilde{\mathbf{H}}\mathbf{f} + \mathbf{H}(\mathbf{G}\mathbf{f} - \mathbf{b})\|^2 \quad \text{subject to } \tilde{\mathbf{I}}\mathbf{f} = \mathbf{0}, \tag{10}$$

where $\tilde{\mathbf{I}}$ is a diagonal matrix with ones on the diagonal entries corresponding to the control points and zeros for the other diagonal entries.

I use a preconditioned CG method (Wu and Hale, 2015b; Wu et al., 2016) to solve this linear system with hard constraints. The constraint equation $\tilde{\mathbf{I}}\mathbf{f} = \mathbf{0}$ is implemented with simple preconditioners in the CG method; the details of constructing such preconditioners are discussed by Wu and Hale (2015b). Beginning with an initial indicator function $f(\mathbf{x}) = 0$ that satisfies the constraint equation $\tilde{\mathbf{I}}\mathbf{f} = \mathbf{0}$, the CG iterations gradually update the function for all samples, whereas the preconditioners guarantee that the updated function always satisfies the constraint equation after each iteration.

Figure 7 shows an example of salt indicator functions computed with and without control points by solving equations 9 and 10, respectively. In Figure 7b, the zero contour of the salt indicator function exactly passes through the control points, as expected. In areas away from the control points, the zero contour with control points shown in Figure 7d coincides with the one without control points shown in Figure 7c. Different interpreters might provide different interpreted control points for the same salt, but this example demonstrates that the results of the method can honor human interactions and automatically computed salt attributes. The human interactions can be picked curves or surface patches, which can be incorporated as sets of control points for the method to provide even stronger control than single points.

CONCLUSIONS

The methods proposed in this paper comprise a two-step process to first compute a salt likelihood image and then compute a salt indicator function, which is used to extract salt boundaries. I tried to ignore the second step and directly extract salt boundaries from a salt likelihood image computed in the first step. However, the extracted salt boundaries were often noisy and were incomplete segments or patches.

In the first step, I computed salt likelihood as an attribute that evaluates the variations in reflector linearity or planarity in directions perpendicular to seismic reflectors. A better way might be to try all possible directions and use the maximum variation in linearity or planarity as the salt likelihood. However, this might take much more time to compute a salt likelihood image.

The second step is important for computing smooth and closed salt boundaries, especially when the input salt samples are noisy or incomplete. For the second step, any salt attributes other than the salt likelihood can also be used to compute a similar salt indicator function for salt boundary extraction. Manually interpreted points, segments, or surface patches can be used as constraints in this second step to compute a more reliable salt indicator function and therefore obtain more reasonable salt boundaries. The proposed method provides an especially simple way to specify such constraints by interactively picking points at salt boundaries. This method can be implemented to interactively add or move control points, while quickly updating the salt indicator function and extracted salt boundaries.

Most of the computation time in this two-step process is spent in the first step on constructing the structure tensor field because relatively computationally expensive structure-oriented smoothing filter is applied to each element of the tensor field. My implementation of the whole process requires less than 20 min to process the 3D example ($242 \times 611 \times 591$) on an eight-core computer.

ACKNOWLEDGMENTS

In much of the research described in this paper, I benefited greatly from discussions with D. Hale and S. Fomel. This research is jointly supported by the sponsors of the Consortium Project on Seismic Inverse Methods for Complex Structures, and the Texas Consortium for Computational Seismology. The seismic images used in this paper are a subset of F3 seismic data provided by dGB Earth Sciences B.V. through OpendTect.

REFERENCES

Amin, A., and M. Deriche, 2015, A hybrid approach for salt dome detection in 2D and 3D seismic data: IEEE International Conference on Image Processing (ICIP), 2537–2541.

Aqrawi, A. A., T. H. Boe, and S. Barros, 2011, Detecting salt domes using a dip guided 3D Sobel seismic attribute: 81st Annual International Meeting, SEG, Expanded Abstracts, 1014–1018.

Asjad, A., and D. Mohamed, 2015, A new approach for salt dome detection using a 3D multidirectional edge detector: Applied Geophysics, **12**, 334–342, doi: 10.1007/s11770-015-0512-2.

Berger, M., A. Tagliasacchi, L. Seversky, P. Alliez, J. Levine, A. Sharf, and C. Silva, 2014, State of the art in surface reconstruction from point clouds: EUROGRAPHICS star reports, 161–185.

Berthelot, A., A. H. Solberg, and L.-J. Gelius, 2013, Texture attributes for detection of salt: Journal of Applied Geophysics, **88**, 52–69, doi: 10.1016/j.jappgeo.2012.09.006.

Deriche, R., 1993, Recursively implementating the Gaussian and its derivatives: Research Report RR-1893, INRIA.

Donoho, D. L., M. Vetterli, R. A. DeVore, and I. Daubechies, 1998, Data compression and harmonic analysis: IEEE Transactions on Information Theory, **44**, 2435–2476, doi: 10.1109/18.720544.

Fehmers, G. C., and C. F. Höcker, 2003, Fast structural interpretation with structure-oriented filtering: Geophysics, **68**, 1286–1293, doi: 10.1190/1.1598121.

Guennebaud, G., and M. Gross, 2007, Algebraic point set surfaces: Presented at the ACM SIGGRAPH 2007 Papers, ACM.

Hale, D., 2006, Recursive Gaussian filters: CWP-546.

Hale, D., 2009, Structure-oriented smoothing and semblance: CWP Report 635.

Hale, D., 2013, Methods to compute fault images, extract fault surfaces, and estimate fault throws from 3D seismic images: Geophysics, **78**, no. 2, O33–O43, doi: 10.1190/geo2012-0331.1.

Halpert, A., and R. G. Clapp, 2008, Salt body segmentation with dip and frequency attributes: Stanford Exploration Project, 113.

Halpert, A. D., R. G. Clapp, and B. Biondi, 2014, Salt delineation via interpreter-guided 3D seismic image segmentation: Interpretation, **2**, T79–T88, doi: 10.1190/INT-2013-0159.1.

Haukås, J., O. R. Ravndal, B. H. Fotland, A. Bounaim, and L. Sonneland, 2013, Automated salt body extraction from seismic data using the level set method: First Break, **31**, 35–42, doi: 10.3997/1365-2397.2013009.

Hegazy, T., and G. Alregib, 2014, Texture attributes for detecting salt bodies in seismic data: 84th Annual International Meeting, SEG, Expanded Abstracts, doi: 10.1190/segam2014-1512.1.

Jing, Z., Z. Yanqing, C. Zhigang, and L. Jianhua, 2007, Detecting boundary of salt dome in seismic data with edge-detection technique: 77th Annual International Meeting, SEG, Expanded Abstracts, 1392–1396.

Kazhdan, M., M. Bolitho, and H. Hoppe, 2006, Poisson surface reconstruction: Proceedings of the fourth Eurographics Symposium on Geometry Processing.

Kazhdan, M., and H. Hoppe, 2013, Screened Poisson surface reconstruction: ACM Transactions on Graphics (TOG), **32**, 1–13, doi: 10.1145/2487228.

Lipman, Y., D. Cohen-Or, D. Levin, and H. Tal-Ezer, 2007, Parameterization-free projection for geometry reconstruction: ACM Transactions on Graphics (TOG), **26**, 22, doi: 10.1145/1276377.

Lomask, J., R. G. Clapp, and B. Biondi, 2007, Application of image segmentation to tracking 3D salt boundaries: Geophysics, **72**, no. 4, P47–P56, doi: 10.1190/1.2732553.

Lorensen, W. E., and H. E. Cline, 1987, Marching cubes: A high resolution 3D surface construction algorithm: ACM Siggraph Computer Graphics, **21**, 163–169, doi: 10.1145/37402.

Ramirez, C., G. Larrazabal, and G. Gonzalez, 2016, Salt body detection from seismic data via sparse representation: Geophysical Prospecting, **64**, 335–347, doi: 10.1111/gpr.2016.64.issue-2.

Shi, J., and J. Malik, 2000, Normalized cuts and image segmentation: IEEE Transactions on Pattern Analysis and Machine Intelligence, **22**, 888–905, doi: 10.1109/34.868688.

Van Vliet, L., I. Young, and P. Verbeek, 1998, Recursive Gaussian derivative filters: Proceedings of the 14th International Conference on Pattern Recognition, 509–514.

Van Vliet, L. J., and P. W. Verbeek, 1995, Estimators for orientation and anisotropy in digitized images: Proceedings of the first annual conference of the Advanced School for Computing and Imaging ASCI'95, 442–450.

Wang, Z., T. Hegazy, Z. Long, and G. AlRegib, 2015, Noise-robust detection and tracking of salt domes in postmigrated volumes using texture, tensors, and subspace learning: Geophysics, **80**, no. 6, WD101–WD116, doi: 10.1190/geo2015-0116.1.

Weickert, J., 1997, A review of nonlinear diffusion filtering, *in* B. ter Haar Romeny, L. Florack, J. Koenderink, and M. Viergever, eds., Scale-space theory in computer vision: Springer Berlin Heidelberg, Lecture Notes in Computer Science 1252, 3–28.

Wu, X., and D. Hale, 2013, Extracting horizons and sequence boundaries from 3D seismic images: 83rd Annual International Meeting, SEG, Expanded Abstracts, 1440–1445.

Wu, X., and D. Hale, 2015a, 3D seismic image processing for unconformities: Geophysics, **80**, no. 2, IM35–IM44, doi: 10.1190/geo2014-0323.1.

Wu, X., and D. Hale, 2015b, Horizon volumes with interpreted constraints: Geophysics, **80**, no. 2, IM21–IM33, doi: 10.1190/geo2014-0212.1.

Wu, X., and D. Hale, 2016, 3D seismic image processing for faults: Geophysics, **81**, no. 2, IM1–IM11, doi: 10.1190/geo2015-0380.1.

Wu, X., S. Luo, and D. Hale, 2016, Moving faults while unfaulting 3D seismic images: Geophysics, **81**, no. 2, IM25–IM33, doi: 10.1190/geo2015-0381.1.

Wu, X., and G. Zhong, 2012, Generating a relative geologic time volume by 3D graph-cut phase unwrapping method with horizon and unconformity constraints: Geophysics, **77**, no. 4, O21–O34, doi: 10.1190/geo2011-0351.1.

Zhang, Y., and A. D. Halpert, 2012, Enhanced interpreter-aided salt boundary extraction using shape deformation: 82nd Annual International Meeting, SEG, Expanded Abstracts, doi: 10.1190/segam2012-1337.1.